New eastern China agricultural burning fire emission inventory and trends analysis from combined geostationary (Himawari-8) and polar-orbiting (VIIRS-IM) fire radiative power products

Tianran Zhang[1, 2], Mark C. de Jong[1, 2], Martin J. Wooster[1, 2], Weidong Xu[1, 2], Lili Wang[3]

[1] King's College London, Department of Geography, Strand, London WC2R 2LS.

[2] NERC National Centre for Earth Observation (NCEO)

[3] LAPC, Institute of Atmospheric Physics, Chinese Academy of Sciences, Beijing 100029, PR China

Correspondence to: Tianran Zhang (tianran.zhang@kcl.ac.uk)

Abstract

Open burning of agricultural crop residues is widespread across eastern China, and during certain post-harvest periods this activity is believed to significantly influence air quality. However, the exact contribution of crop residue burning to major air quality exceedances and air quality episodes has proven difficult to quantify. Whilst highly successful in many regions, in areas dominated by agricultural burning MODIS-based fire emissions inventories such as GFAS and GFED are suspected of significantly underestimating the magnitude of biomass burning emissions due to the typically very small, but highly numerous, fires involved that are quite easily missed by coarser spatial resolution remote sensing observations. To address this issue, we here use twice daily fire radiative power (FRP) observations from the 'small fire optimised' VIIRS-IM FRP product, and combine it with fire diurnal cycle information taken from the geostationary Himawari-8 satellite. Using this we generate a unique high spatio-temporal resolution agricultural burning inventory for eastern China for the years 2012-2015, designed to fully take into account small fires well below the MODIS burned area or active fire detection limit, focusing on dry matter burned (DMB) and emissions of CO_2, CO, $PM_{2.5}$ and black carbon. We calculate DMB totals 100 to 400% higher than reported by GFAS and GFED4.1s, and quantify interesting spatial and temporal patterns previously un-noted. Wheat residue burning, primarily occurring in May-June, is responsible for more than half of the annual crop residue burning emissions of all species, whilst a secondary peak in autumn (Sept-Oct) is associated with rice and corn residue burning. We further identify a new winter (Nov-Dec) burning season, hypothesised to be caused by delays in burning driven by the stronger implementation of residue burning bans during the autumn post-harvest season. Whilst our emissions estimates are far higher than those of other satellite-based emissions inventories for the region, they are lower than estimates made using traditional 'crop yield-based approaches' (CYBA) by a factor of between 2 and 5x. We believe that this is at least in part caused by outdated and overly high burning ratios being used in the CYBA approach, leading to the

32   overestimation of DMB. Therefore we conclude that that satellite remote sensing approaches which adequately detect

33   the presence of agricultural fires are a far better approach to agricultural fire emission estimation.

34

35   **Keywords**: Agriculture, Biomass Burning, Active Fire, VIIRS, Air Quality, Fire Emission

36

1. INTRODUCTION

38   Eastern China (111 - 123 ºE, 27 – 40 ºN) is home to around one third of the Chinese population and includes the area

39   of the North China Plain and the Yangtze Plain - two of the largest agricultural zones in China (Fig. 1). Cropland

40   covers over 1.7 million km^2 of eastern China, and the region is responsible for an estimated 25% of China's crop

41   production, including around 51% of the national rice yield (NBSC, 2012). Large amounts of crop residue (~ 60

42   Tg/year including stems, stalks, straw etc) results from this agricultural production (Chen et al., 2017; Huang et al.,

43   2012; Zhang et al., 2015), and the burning of this waste in open fields is widespread across much of eastern China

44   (Fig. 2).

45   This biomass burning has both local and regional scale air quality impacts, with emissions of particulate matter (PM)

46   of particular concern (Bond et al., 2013). The East Asian monsoon system that influences much of mainland China

47   results in prevailing north-westerly to south-easterly atmospheric transport during winter, which is reversed in the

48   summer months. Under these influences, the smoke from agricultural residue fires in Eastern China often affects

49   "mega-cities" like Beijing and Shanghai (Chan & Yao, 2008; Cheng et al., 2013; Du et al., 2011; Li et al., 2010).

50   Modelling studies show that these agricultural emissions can drive intense regional air pollution episodes; Huang et

51   al. (2012) suggest that PM_{10} concentrations in some cities could reach 600 µg m^{-3} during such episodes, a level 6×

52   higher than the WHO 24h-mean PM_{10} air quality guideline for human health (WHO, 2005).

53   Agricultural burning in eastern China accounts for a significant part of China's total biomass burning emissions

54   (Streets et al., 2003; Chen et al., 2017), however the specific contribution of crop residue burning to air quality

55   exceedances in China remains uncertain, partly because there is considerable doubt as to the amount of dry matter

56   burned (DMB) in crop residue fires. For example, his leads to a ~450 % range in total crop residue burning black

57   carbon emissions in Asia between different emissions inventories (Streets et al., 2003), while emissions estimates of

58   gaseous species are similarly varied.

59   A major source of this uncertainty stems from the hitherto relatively poor ability of earth observation (EO) satellite

60   instruments to adequately detect biomass burning activity in many agricultural areas due to the small size of the fires

61   usually found in these areas. Many agricultural fields in eastern China are typically only around 700 m^2 in area (NBSC,

62   2012), and fires ignited to burn across the stubble left in the place after harvest are therefore hard to detect with

63   moderate spatial resolution burned area (BA) mapping from sensors such as MODIS, and are made even more elusive

64   by the common farming practice of pilling up residues into an even smaller area before igniting them (Zhang et al.,

65   2017; 2018). As mostly BA mapping methods require ~ > 20 % of a pixel to be burned in order for it to be classified

Atmospheric
Chemistry
and Physics
Discussions
Open Access
EGU

66 as 'fire affected' (Giglio et al., 2006; 2009), BA-based emissions inventories such as GFED tend to significantly

67 underestimate fire activity in areas such as eastern China (Zhang et al., 2018).

68 Infrared based Active fire (AF) based detection techniques can discriminate fires covering only 0.01-0.1 % of a pixel

69 area (Wooster et al., 2005; Schroeder et al., 2014), and as such should in theory be able to capture far more fire activity

70 in agricultural areas than BA based methods. Nevertheless, due to the extremely small size of agricultural fires in

71 eastern China, a large proportion of fire activity remains undetected by AF detection algorithms applied to 'moderate'

72 spatial resolution imagery (from sensors such as MODIS). This limitation is a key source of uncertainty within the

73 FRP approach, and indeed in fact can lead to biased (underestimated) FRP totals caused by the non-detection of the

74 lower FRP component of a regions fire regime (e.g. Roberts et al., 2015). Higher spatial resolution polar-orbiting

75 sensors such as VIIRS can provide the ability to identify an increased number of AFs having lower FRP values,

76 particularly when used with algorithms optimised for small fire detection (Zhang et al., 2017) (Fig. 2), but they still

77 only capture fires burning in clear skies at the time of the satellite overpass (Giglio et al., 2003; 2006). This limitation

78 is also a considerable source of uncertainty, and a hinderance given the sometimes short duration of active burning

79 (especially of agricultural fires) and the typical polar orbiting imaging frequency of only a few times per day. To cope

80 with this issue, FRP-based emissions inventories such as GFAS based upon AF methods are generally required to

81 make assumptions or exploit additional data on the timing and relative diurnal variability of fire activity occurring

82 between polar orbiting overpasses in order to estimate, for example, total daily Fire Radiative Energy (FRE) (Kaiser

83 et al., 2012; Xu et al., 2017; Zhang et al., 2017). Here we provide this additional information by exploiting new fire

84 diurnal cycle information taken from the geostationary satellite Himawari-8, combining it with twice daily FRP

85 information provided by the 'small fire optimised' VIIRS-IM product of Zhang et al. (2017) to produce a unique high

86 spatio-temporal resolution agricultural fire dataset (referred to hereafter as the VIIRS-IM/Him dataset) for eastern

87 China based on FRE totals. This new inventory is designed to reduce bias and uncertainty caused by use of one FRP

88 data type alone, and to account for small fires burning even for short periods and often well below the MODIS AF

89 and BA detection limit. The fuel for these fires is waste straw and other agricultural residues, and we use a crop

90 rotation map to classify the type of agricultural residue being burned at each observed location and time. It is then

91 used to select the most appropriate smoke emissions factor for calculating the final fire emissions totals from FRE

92 derived estimates of dry matter burned (DMB).

93

94 **2. DATASETS**

95 2.1 Polar Orbiting VIIRS-IM FRP Product

96 The Visible Infrared Imaging Radiometer Suite (VIIRS) instrument is currently flown aboard the polar orbiting Suomi
97 NPP (since 2011) and NOAA-20 (since 2017) satellites and expands upon the capabilities of the AVHRR and MODIS
98 instruments for environmental monitoring (Zhou et al., 2019). VIIRS has 22 channels spanning the visible to the
99 longwave infrared, a 3000 km swath width, and nadir pixel resolution ranging between 375 m and 750 m (Goldberg
100 et al., 2013). Furthermore, a 'pixel aggregation' scheme is applied to VIIRS which limits pixel area increase with scan
101 angle to a maximum of 4× compared to MODIS' 10× (Wolfe et al., 2013).

102 With a necessary emphasis on the detection of small fires typical of agricultural regions, our work focuses on
103 generating a gridded daily biomass burning fuel consumption product that estimates DMB and emissions from the
104 VIIRS-IM AF Detection and FRP product developed and optimised for eastern China by Zhang et al. (2017), using
105 data from the instrument aboard the Suomi NPP satellite with a mean local daytime overpass time of 13:30 in the
106 ascending node, and a mean local nighttime overpass time of 01:30 in the descending node (Wolfe et al., 2013). Fig.
107 2 shows an example of the VIIRS-IM FRP product, generated from the two observations per day provided by Suomi
108 NPP VIIRS. This FRP product blends the advantages of the 'small fire' sensitivity of the VIIRS 375 m I-Band, with
109 the ability to retrieve fire radiative power (FRP) over larger fires using the 750 m M-Band observations. Due to the
110 very small size of agricultural fires in China, and because the VIIRS I-Band pixel area is 10× smaller than the pixel
111 area of MODIS, far more fires can be detected in eastern china using the VIIRS-IM AF product of Zhang et al. (2017)
112 than can be identified in near simultaneous MODIS data, and on average across eastern China retrieves FRP totals
113 around 4× higher (Zhang *et al.*, 2017).

114

115 2.2 Geostationary Himawari FRP Product

116 To convert the twice-daily VIIRS-IM FRP product to daily-integrated FRE, information on the fire diurnal cycle is
117 required (Ellicott et al., 2009; Freeborn et al., 2008; Roberts et al., 2009). We obtained this from 10-min temporal
118 resolution observations from the geostationary Himawari-8 satellite, whose data have recently been used to derive AF
119 detections and FRP metrics across Asia by Xu et al. (2017). Himawari cannot be used in isolation to directly estimate
120 daily FRE for each of the 4-years of the study, because (i) Himawari data are only available from early 2015 onwards,
121 and (ii) Himawari's relatively coarse pixel size (2 km at the sub-satellite point) means that it omits even more of the
122 agricultural fires than does MODIS (as illustrated by Xu et al., 2017 and in Fig.3). However, where agricultural fires
123 are concentrated in sufficient density, observations by Himawari do enable their detection and these data can be used
124 to map the changing FRP of these fires over the day for derivation of the fire diurnal cycle.

125

126 2.3 Crop Rotation Map

127   The predominant agricultural residues burned across eastern China are wheat, corn and rice straw (Huang et al., 2012).

128   To classify the likely residue type of each detected fire, a crop rotation map (Fig. S1) was generated from the

129   MIRCA2000 0.08° global monthly crop area dataset (Portmann *et al.,* 2010), which has a spatial resolution equivalent

130   to 9.2 km × 9.2 km at the equator. These data were used to assign fire activity to a particular crop residue type, which

131   determined the appropriate agricultural biomass burning emission factors to apply (see Section 3.3).

132

133   2.4 Land Cover Data

134   We use the GlobeLand30 land cover product (Chen et al, 2015) to classify land cover/use for our study area in Eastern

135   China. GlobeLand30 provides 30m spatial resolution land cover data for a baseline year of 2010 derived primarily

136   from Landsat (TM5 & ETM +) and China Environmental Disaster Alleviation Satellite (HJ-1) imagers. Fig. 1 shows

137   the spatial distribution of the agricultural land ratio (regridded to 0.01 degree spatial resolution) calculated use this

138   dataset in eastern China.

139

140   2.5 GFED & GFAS Emissions Inventory Data

141   The results from the combined VIIRS-IM and Himawari FRP based emissions (VIIRS-IM/Him) dataset were

142   compared to two state-of-the-art global fire emission databases, the Global Fire Emissions Database (GFED) and the

143   Global Fire Assimilation System (GFAS). GFED was built to combine remotely sensed data on BA with fuel loads

144   from the CASA biogeochemical model of vegetation growth, producing monthly, spatially explicit pyrogenic fuel

145   consumption, carbon, GHG and air pollution emission estimates at 0.25° grid cell resolution globally (Van der Werf

146   et al., 2010; Giglio et al., 2013). The most recent version (GFED4.1s) includes a "small fire boost" based on AF

147   detections, in an attempt to counteract the inability of the MODIS BA product to detect many agricultural fires

148   (Randerson et al., 2012; Van der Werf et al., 2017). Due to this 'boost' GFED4.1s shows higher values of dry matter

149   burned (DMB) in most eastern China grid cells compared to the 'unboosted' GFED4, and a more extensive fire

150   distribution. However, Zhang et al. (2018) show that the boosting procedure can introduce significant anomalies into

151   the GFED dataset at certain times of year, generated when MODIS' AF detection procedure incorrectly identifies

152   urban features in eastern China as fires.

153   In contrast to GFED, the GFAS fire emissions database is based on AF detections and is integrated into Copernicus

154   Atmosphere Monitoring Service (CAMS) system for near-real-time atmospheric composition monitoring and

155   forecasting. Developed by Kaiser et al. (2012) and based on the FRP method, MODIS supplies the FRP data for the

156   current GFAS v1.2 up to 4 times per day at most latitudes. From these observations, DMB is calculated via a regression

157   against GFED DMB values (Kaiser et al., 2012) and daily emissions of 40 emitted species are then calculated at 0.1°

158   spatial resolution.

159

160   2.6 Crop Yield Based Approach Emissions Inventory Data

161   The traditional method for estimation of agricultural fire emissions is the so-called crop yield based approach (CYBA),

162   and we compare data from such approaches to our new VIIRS-IM/Him methodology. CYBAs typically calculate the

163   amount of crop residue burned in a region using a combination of crop production statistics and related additional

164   parameters using following equation:

165    $DMB = \sum_{i=1}^{n} P_i R_i B_i C$ (1)

166   Where i stands for each of n different crops; DMB is total dry matter burned (kg) in the region; P_i is the regional

167   production of crop i (kg), and is usually derived from annual agricultural statics reports; R_i is the dry matter production-

168   to-residue ratio (unitless), which depends on the crop type i; B_i is the proportion of residue burned in the field for crop

169   type i in the region under study (i.e. the 'burning ratio'; 0-1, unitless); and C is crop combustion completeness (0-1,

170   unitless, Huang *et al.,* 2012). DMB is then multiplied by appropriate particulate/gaseous emission factors in order to

171   estimate the total emissions from agricultural burning.

172   Certain of the parameters of Eqn. 1 are not so easily determined. For example, the burning ratio (B_i) is often based on

173   questionnaires or investigations on the use of crop residues conducted with farmers (Gao *et al.,* 2002; Wang and Zhang,

174   2008). Because of strong variations in socio-economic development across the huge expanse of mainland China, large

175   differences in the estimates of B_i exist (Jiang *et al.,* 2012; Liu *et al.,* 2008; Yamaji *et al.,* 2010). B_i may also change

176   considerably from year to year since it is strongly impacted by the level of local economic development, the

177   availability of alternative uses for crop residues in the region, and the regional governance of fire prohibition (Chen

178   *et al.,* 2017). Moreover, considering the official prohibition of open air burning, the reliability of data based on surveys

179   that ask farmer how much residue they burn is questionable. Despite this, most studies that include estimation of

180   agricultural fire emissions in Eastern China have relied on the CYBA (e.g. Cao *et al.,* 2006; He *et al.,* 2011; Huang *et*

181   *al.,* 2012; Li *et al.,* 2009; Qin and Xie, 2011; Yan *et al.,* 2006; Zhao *et al.,* 2015).

182

183   **3. METHODOLOGY**

184   3.1 Data Gridding and Cloud Cover Adjustment

185   The VIIRS-IM FRP product data (in MW), originally derived at the pixel scale, were aggregated to 0.1° resolution for

186   this analysis. Unlike the daily average MODIS FRP calculation of GFAS, which weights individually contributing

187   MODIS FRP observations by their view zenith angle to downgrade the importance of far off-nadir measurements

188   (Kaiser *et al.,* 2012), no such weighting was applied to the VIIRS-IM FRP data since they have already shown very

189   limited view zenith angle dependence as a result of the VIIRS' pixel-averaging procedure (Zhang et al., 2017). For

190   each VIIRS overpass, the total observed FRP present in each 0.1° grid cell j (i.e. FRP$_j$) was calculated from the

191   cumulative FRP of all native resolution AF pixels i within the grid cell:

192    $FRP_j = \sum_{i \in j} FRP_i$ (2)

193 Total observed agricultural area (A, excluding cloud covered area) within each 0.1° grid cell was calculated similarly

194 using the GlobeLand30 30m landcover map:

195 $A_j = \sum_{i \in j} A_i$ (3)

196 The VIIRS-IM product is only affected to a limited degree by smoke because of the relative transparency of smoke

197 plumes at Mid-Wave Infrared (MWIR) wavelengths due to the dominant particle size being smaller than the

198 wavelengths of the VIIRS MWIR channel (Zhang et al., 2017). However, the product cannot provide information in

199 cloud covered areas, and so an adjustment is required to take into account actively burning fires hidden from view by

200 clouds. Following Streets *et al.* (2003) we assume that for partially cloud covered grid cells, the AF and FRP

201 distribution under cloud is the same as under the clear sky areas, as is also assumed in GFAS (Kaiser *et al.*, 2012).

202 Subsequently, the gridded and cloud-adjusted FRP areal density (ρ_j, MW.km^{-2}) is calculated using:

203 $\rho_j = \frac{FRP_j}{A_j}$ (4)

204

205 3.2 Diurnal Cycle and Daily FRE Generation

206 Hourly averages of the 10-minute FRP data from the Himawari-8 FRP product of Xu *et al.* (2017) were gridded to the

207 same 0.1° grid cell resolution as the VIIRS-IM dataset. For each grid cell and calendar day, hourly FRP data were

208 normalised in order to minimise the impact of day-to-day variations in fire activity:

209 $\widetilde{FRP_{j,d}^h} = \frac{FRP_{j,d}^h - \min(FRP_{j,d})}{\max(FRP_{j,d}) - \min(FRP_{j,d})}$ (5)

210 Where $\widetilde{FRP_{j,d}^h}$ is the normalised Himawari-8 FRP for hour h on day d for grid cell j; $FRP_{j,d}^h$ is the observed Himawari-

211 8 FRP (MW) for hour h on day d for grid cell j; $\max(FRP_{j,d})$ and $\min(FRP_{j,d})$ are respectively the maximum and

212 minimum hourly Himawari-8 FRP (MW) observed on day d for grid cell j. Note that h is in local time (UTC/GMT +

213 8 hours) and the diurnal cycle runs from 0 to 23 hours.

214 $\widetilde{FRP_{j,d}^h}$ data for 2015 were used to produce two normalised 'seasonal' diurnal fire cycles for the eastern China study

215 area: a 'summer' diurnal cycle, constructed from May-June data, and an 'autumn' diurnal cycle, constructed from

216 Sept-Oct data. Both normalised seasonal diurnal cycles were calculated using a weighted mean so that days and grid

217 cells with high fire activity had the greatest influence on the cycle:

218 $$FRP^h = \frac{\sum_d \sum_j \left(\widetilde{FRP_{j,d}^h} \times FRP_{j,d}^h \right)}{\sum_d \sum_j \left(FRP_{j,d}^h \right)}$$ (7)

219

220 Where FRP^h is the normalised FRP for hour h for the entire study area and fire season (summer or autumn). Fig. 4

221 shows the resulting weighted mean fire diurnal cycle for the summer season for Eastern China. This diurnal cycle is

222   bi-modal: a primary peak occurs around 13:00 local time that extends from around 08:00 to 18:00 (daytime) and a

223   second much smaller peak occurs around 21:00 local time (with a height of only ~ 20% of the normalised FRP value

224   of the first peak).

225   We blended information from the Himawari FRP diurnal cycle with the instantaneous twice-daily VIIRS-IM FRP

226   areal density (ρ_j, MW.km^{-2}) data, using an approach based on Andela et al. (2015) to create the VIIRS-IM/Him dataset.

227   Here we represent the diurnal fire cycle as a gaussian function parameterised using the Himawari FRP diurnal cycle,

228   superimposed on a fixed baseline. For a given grid cell j, at instantaneous time t, VIIRS-IM/Him FRP areal density is

229   calculated by:

230

231
$$\rho_{VIIRS-Him_{j,t}} = \rho_{VIIRS_{night,j}} + \mu\left(\rho_{VIIRS_{day,j}} - \rho_{VIIRS_{night,j}}\right) e^{-\frac{(t - t_{Himpeak})^2}{2\sigma^2}} \qquad (8)$$

232

233   Where $\rho_{VIIRS-Him_{j,t}}$ is the instantaneous VIIRS-IM/Him FRP areal density (MW.km^{-2}) for grid cell j at time t;

234   $\rho_{VIIRS_{night,j}}$ is the night-time (~01:00 LST) VIIRS-IM FRP areal density value (MW.km^{-2}) for grid cell j; $\rho_{VIIRS_{day,j}}$

235   is the day time (~13:00 LST) VIIRS-IM FRP areal density value (MW.km^{-2}) for grid cell j; μ is an adjustment factor

236   used to account for the difference between the VIIRS daytime overpass time and the peak time of the weighted mean

237   fire diurnal cycle (see below); $t_{Himpeak}$ is the time of day at which the seasonal Himawari FRP diurnal cycle peaks; σ is

238   the standard deviation of the main peak of the Himawari FRP diurnal cycle, calculated by fitting a gaussian function

239   (using non-linear least squares) to the seasonal Himawari FRP diurnal cycles. The summer diurnal cycle σ value

240   (2.39±0.053) was applied during the April-August period, and the autumn diurnal cycle σ value (1.63±0.041) was

241   applied during the September-March period.

242   The adjustment factor μ is used to account for the fact that the VIIRS daytime overpass time is unlikely to coincide

243   with the peak of the fire diurnal cycle:

244

245
$$\mu = e^{\frac{\left(t_{VIIRS_{day,j}} - t_{Himpeak}\right)^2}{2\sigma^2}} \qquad (9)$$

246

247   Where $t_{VIIRS_{day,j}}$ is the local time of the VIIRS-IM FRP observation for grid cell j.

248   Daily FRE was then calculated for each grid cell j and calendar day by integrating the instantaneous VIIRS-IM/Him

249   FRP data using Eqn. 8.

250

251   3.3 Conversion to Dry Matter Burned (DMB) and Smoke Emissions

252   To convert the calculated FRE areal density to fuel consumption/DMB, we multiplied FRE by the 0.368 (±0.015)

253    $kg.MJ^{-1}$ factor derived by Wooster *et al*. (2005) from a series of outdoor experimental straw fires, that were very

254   similar to the Chinese agricultural residue fires used herein (Zhang et al., 2015). To convert the resultant DMB into

255   smoke emissions, we used the emission factors of wheat and rice derived from *in situ* measurements in agricultural

256   areas by Zhang et al. (2015) (Table 1). Corn residue was not a fuel type measured during those experiments, and so

257   for this fuel type (which was only 16-22% of the total agricultural fuel consumption) we used the emissions factors

258   for agricultural corn fires from Andreae and Merlet (2001), as is used in GFAS (Kaiser *et al.,* 2012) (Table 1). Together

259   with the crop rotation map (see Section 2.3 and Fig. S1) the EFs from Table 1 enabled us to select the appropriate

260   emissions factor for use at a particular location and time of year.

261   Furthermore, a winter burning season was discovered during November and December (see details in Section 5.1)

262   when no cultivation crop is shown in the MIRCA2000 data in the study region. Analysis in this study shows that

263   winter fires are likely to result from the combustion of stored residues from the autumn harvest season, therefore all

264   fire activity in winter was assigned to crop types (and therefore emission factors) using the crop rotation map from the

265   previous closest month (October) (Fig. S1). This methodological change is accounted for in the data presented in Fig.

266   5.

267

268   **4. BIOMASS BURNING AND EMISSIONS RESULTS**

269   4.1 Temporal and Spatial Distribution of FRE In Eastern China

270   Fig. 5 shows the time series of daily mean FRE areal density in eastern China from February 2012 to December 2015,

271   reported at 0.1° grid cell resolution, and broken down into three main crop residue types. A strong seasonal variation

272   is seen, with peak activity in summer (May-June) associated with wheat residue burning and a smaller secondary peak

273   in activity occurring in autumn (Sept-Oct) associated with corn and rice residue burning. In fact, the secondary peak

274   is a combination of several fluctuations lasting from October until December, further discussed in Section 5.1. Over

275   the whole 4-year period, wheat crop residues contributed 65% of the total FRE, rice residues 18%, and corn residues

276   17%.

277   A distinct spatial pattern showing two main burning seasons can also been seen when FRE areal density is mapped

278   (Fig. 6). During the summer burning season (May-June), most fires are located between 32°N - 36°N, extending from

279   112°E - 120°E near the coast. In the autumn season (Sept-Oct), less fire activity occurs than in the summer fire season

280   and it is more evenly distributed across the entire study area, though there is still a focus of fire activity between 32 -

281   34°N and 112 - 119°E. Moreover, in the southwest of the study area (29 - 32°N and 112 - 114°E) we see a region

282   that only appears to undergo substantial burning in the autumn. This is located in the centre of Hubei Province, which

283   contributes around 12% of the total rice yield of the whole of China (NBSC, 2015). This area contributes to between

284   10 and 18 % (year dependant) of the total autumn burning season FRE.

285

286   4.2 DMB Comparisons to GFAS and GFED

287   The outputs generated by our combined VIIRS and Himawari processing chain were compared to those of GFAS and

288   GFED4.1s (Fig. 7). Dry matter burned (DMB) was used as the common comparison metric, as this removes differences

289   arising from the use of different emissions factors within the inventories. Overall, the VIIRS-IM/Him DMB estimates

290   are around 2× to 5× higher than those reported for corresponding months by GFAS and GFED 4.1s. As detailed in

291   Zhang et al. (2017) and discussed in Section 2, VIIRS has the ability to detect far smaller (and lower FRP) fires than

292   MODIS, due to its far smaller pixel size and the fact that the I-band observations also retain their pixel area more

293   effectively across the swath. Ultimately, this difference results in far higher DMB being obtained by the VIIRS-

294   IM/Him inventory compared to the MODIS based GFAS and GFED inventories.

295   During the summer months of May-June, all three inventories (GFAS, GFED and VIIRS-IM/Himawari) show a clear

296   peak in DMB, but GFAS and VIIRS-IM/Him show a much sharper peak in June, while GFED's summer burning

297   season extends one month earlier (May) and later (July). This extended summer fire season reported by GFED is likely

298   the result false fire reporting, discussed at length in Zhang et al (2018). VIIRS-IM/Him shows a June DMB peak

299   ranging from 3.30 to 11.2 Tg, 2× higher than GFED4.1s (1.89 - 5.34 Tg) and GFAS (2.00 to 4.30 Tg). It should be

300   remembered that the conversion of daily average FRP to DMB in GFAS is derived via a calibration to GFED4.1s

301   (Kaiser *et al.*, 2012), so these two emissions databases understandably report similar monthly DMB totals.

302   For the autumn (Sept-Oct) burning season, the peaks in the GFAS and GFED inventories are much less pronounced

303   than the summer burning season peaks (Fig. 7). DMB in October ranges from 0.57 - 1.74 Tg for GFED, significantly

304   higher than the 0.31 - 0.61 Tg reported by GFAS, but far lower than the 1.62 - 3.05 Tg of the VIIRS-IM/Him inventory.

305   The VIIRS-IM/Him derived DMB estimates for eastern China are thus 2 to 3× higher than GFED4.1s and 5× higher

306   than GFAS; these represent larger differences than exist for the earlier summer burning season. This indicates that

307   agricultural fires burning during the autumn fire season may be on average smaller and/or more isolated from other

308   fires than they are in the summer burning season, and thus are even more likely to be missed by the MODIS AF

309   detection product (Giglio *et al.,* 2006) and/or the MODIS BA product (Giglio *et al.,* 2013) than they are during other

310   more intense burning periods.

311

312   4.3 Agricultural Fire Emissions Intercomparison

313   This section presents a comparison of the total annual agricultural fire emissions calculated using the VIIRS-IM/Him

314   method with other inventories of Chinese agricultural fire emissions in the literature, and against emissions totals from

315   other sectors to gain a better understanding of the relative importance of agricultural fire emissions. To compare with

316   other reported agricultural fire emission inventories for China, the DMB estimates produced herein were converted to

317   fire emissions estimates using the emissions factors and methods described in Section 3.3; these results are summarised

318   in Fig. 8 and Table 2.

319   From Fig. 8, it is clear that wheat residue burning is the primary agricultural emission source, accounting for over 50%

320   of the total emissions released each year (specifically 55-69% of $PM_{2.5}$, 71-81% of BC, 66-77% of CO_2, and 69-80%

321   of CO). Fig. 8 also indicates a considerable reduction in emissions in 2015 compared to previous years, largely

322   attributable to a reduction in the amount of wheat residue burnt. For example, total $PM_{2.5}$ emissions from agricultural

323   residue burning in eastern China for 2012-14 cover a relatively narrow range of 107 - 130 Gg (Fig. 8 & Table 2), but

324   decrease to 67 ± 24 Gg in 2015 due to an almost halving of DMB (Fig. 7); similar patterns are observed for BC, CO_2,

325   and CO (Fig.8).

326   From Table 2, it is apparent that emissions totals calculated using the VIIRS-IM/Him approach are consistently higher

327   than those reported by GFAS by factor of 1.2-4.2 (species/year dependent). Similarly, VIIRS-IM/Him emissions totals

328   for CO_2 and PM2.5 are greater than those reported by GFED by a factor of 1.1-1.7. In both cases, this can be explained

329   by the tendency of MODIS to miss activity from small fires compared to VIIRS. VIIRS-IM/Him emissions for CO

330   and BC in 2015 are lower than those reported for GFED, which can be attributed to differences in the emissions factors

331   used between the approaches.

332   Emissions totals calculated using the VIIRS-IM/Him approach are smaller than those estimated by CYBA studies for

333   the East China/North China Plain regions (Zhang et al., 2008; Huang et al., 2012; Qiu et al., 2016) by a factor of 2-5.

334   It is possible that the much higher totals estimated from the CYBA based studies maybe due to the use of very high

335   residue burning ratios (B_i in Eq. 1) for corn and rice in particular. This finding is discussed further in Section 5.

336   Liu *et al.,* (2015) estimated total emissions in the North China Plain region (a similar area to the study area used in

337   this paper) using MODIS FRP-based calculations, and assumed a modified Gaussian function for the diurnal cycle to

338   generate the daily FRE estimates from which emissions were then derived. These estimates are much closer in

339   magnitude to the equivalent estimates calculated using the VIIRS-IM/Him method than those from the CYBA studies,

340   however 2013 & 2014 estimates by Liu et al. are consistently lower (by a factor of 0.3-0.9); again, we attribute this

341   difference to the fact that MODIS based methods capture less fire activity than our VIIRS-IM/Him approach.

342   Interestingly, Liu *et al.* (2015) estimated far higher emission totals for 2012 compared to 2013 & 2014 and report

343   greater total CO and BC emissions than we do. For example, annual CO_2 emissions in 2012 (26,000 Gg) are $> 2\times$ their

344   reported total emissions for 2013 (9800 Gg) and 2014 (13,000 Gg). However, Liu *et al.*'s processing approach did not

345   provide any adjustment for the impact of the MODIS 'bow-tie' scan geometry effect, which leads to duplicated AF

346   detections and this FRP towards the edge of the MODIS swath, and which was highlighted as significant issue for

347   FRP quantification by Freeborn *et al.* (2008) and Zhang et al. (2017). This is a particular problem in MODIS data

348   from the year 2012, where large amount of duplicated observations have been found towards edge of swath (Fig. S2).

349   This problem has been addressed in GFAS using a scan-angle dependent weighing factor for the MODIS FRP data

350   (Kaiser *et al.,* 2012), as described in Section 2.5, and GFAS' CO_2 emissions from 2012 are only 24% and 10% higher

351   than from 2013 and 2014 respectively, a much more modest increase compared to that reported in Liu *et al.* (2015).

352   Fig. 9 presents a comparison of agricultural emissions calculated using the VIIRS-IM/Him method with emissions

353   from non-biomass burning sources produced by Li et al. (2014) for a sub-area of eastern China (32-36º N, 112-122º

354   E) for the year 2013. We note that crop burning emissions are of relatively little significance when considered on an

355   annual basis; for all four species (CO_2, CO, $PM_{2.5}$, BC), contributions from agricultural residue burning range between

356   0.56% and 2.0% of total annual emissions, with the majority of emissions resulting from industry and residential

357   sources. However, in June when agricultural burning and emissions are at a maximum, residue burning contributes

358   8.1%, 18%, 22% and 20% of total monthly emissions for CO_2, CO, $PM_{2.5}$ and BC respectively, highlighting the strong

359   seasonal impact agricultural burning can have on the emission of species that affect both climate and air quality.

360

361   **5. ANALYSIS AND DISCUSSION**

362   5.1 Importance of Wheat Residue Burning

363   Findings in Section 4 (Fig. 5 & 8) indicate that a larger proportion of wheat residue than corn or rice residue is burnt,

364   for several reasons. First, the yields of these three crop types in Eastern China are relatively similar - in 2015 for

365   example, wheat yield was 10% lower than rice yield, and only 20% higher than corn (Table S1; NBSC, 2015). Second,

366   the dry matter production-to-residue ratio (R_i in Eqn. 1) of wheat is not higher than that of rice or corn (Table S2;

367   Wang and Zhang, 2008). Third, with the exception of black carbon, the emission factors for wheat residues are broadly

368   similar to or smaller than the corresponding rice and corn emission factors. It is unknown why a greater fraction of

369   wheat residue than corn and rice residue is burnt, however, it is possible that local management practices and/or

370   stakeholder priorities differ depending upon the residue type and time of year at which crops are harvested, ultimately

371   impacting the fate of these residues e.g. residues from certain crops maybe valuable as fertiliser (Huang et al., 2012),

372   animal feed or for domestic/local energy production (Chen et al., 2017; Liu et al., 2008).

373

374   5.2 Discovery of A Winter Burning Season

375   As detailed in Section 4.1, small peaks in our dry matter burned (DMB) time-series are apparent in November-

376   December of each year (grey shaded area shown in Fig. 5). Since no mention of such a winter burning season was

377   found in the literature (e.g. Chen *et al.,* 2017; Huang *et al.,* 2012; Zhang *et al.,* 2008), these winter peaks were initially

378   considered to be erroneous and likely caused by VIIRS AF false alarms that had failed to be excluded by the landcover

379   and/or persistent thermal anomaly masking detailed in Zhang et al., (2017). Furthermore, according to the crop rotation

380   map derived from the MIRCA2000 data (Fig. S1), there is no obvious harvesting of wheat, corn, or rice during the

381   winter in eastern China. However, close examination of the original VIIRS data and the VIIRS-IM FRP product

382   generated from it by Zhang et al., (2017) shows that most of the AF pixels detected in eastern China in winter are in

383   fact located in or very close to areas classified as agricultural land (Fig. S3), and are not located close to industrial

384   areas of the type known to cause false AF detections (Zhang et al., 2017), nor do the AF detections appear multiple

385   times in the same month at the same location, as would be expected if they were false alarms generated by non-fire

386   features. It therefore seems highly probable that these AF detections are actually a consequence of true agricultural

387   burning (Fig. S3-5).

388   The most reasonable explanation for the winter AFs appears to be that some of the crop residues from the Sept-Oct
389   (Autumn) harvest season were left idle for a few months and burned in the winter, rather than immediately. Local
390   newspapers, online media and other information sources were consulted, and were found to support the existence of
391   winter residue burning episodes. One example is a report by Jiangsu Province TV station in 5 December 2013, where
392   a huge crop residue burning episode was reported in Hongze (Jiangsu Province), close to the location shown in Fig.
393   S3. Stills from this TV report show flames, thick smoke and extremely poor visibility resulting from the crop residue
394   burning, described in Chinese language subtitles (Fig. S4). Reports of similar episodes were found in different
395   websites/newspapers from across much of eastern China (e.g. Wang and Zhang, 2016; Za, 2015; Zuo, 2015).
396   Subsequent to this confirmation, an explanation as to why this activity may have occurred outside of the normal
397   burning season was sought. According to Yun Xia, a local governor of the Environmental Department in Hefei
398   (interview conducted by Anhui News; Zuo, 2015), the prohibition on agricultural burning started at beginning of
399   September in that area, and continued up until the 20th November. During this period, the local government strongly
400   enforced its polices aiming to restrict agricultural residue burning, and established almost continuous patrols to
401   identify areas likely to host crop residue fires in order to prevent their ignition. However, without a widespread and
402   cost-effective alternative way to dispose of their crop residues, local farmers may simply have stored the residue
403   material and burned it soon after the end of the prohibition period, when the intensive patrol period had ceased. The
404   end of the prohibition period coincides almost exactly with the time of the new winter burning season identified by
405   our VIIRS-IM/Him dataset (Figs. 5- 7).

406   The winter season is important for biomass burning in this area of China, accounting for between 19 and 36 % (year
407   dependant) of the combined autumn and winter FRE total. Based on the crop rotation map (Fig S1), this fire activity
408   was assigned to the burning of both corn and rice residues, with the contribution of each residue to total FRE (and
409   thus DMB) almost equal (49 % and 51 %, average over all years). This split by residue type is very similar to that
410   observed in the Autumn burning season (corn = 54 %, rice = 46 %, average over all years), despite the observed
411   variation in the spatial distribution of fire between autumn and winter (Fig. 6). In general, winter burning appears to
412   take place closer to provincial capitals than autumn burning does; the reason for this spatial shift in fire is discussed
413   in Section 5.4.

414

415   5.3 Disagreement Between Satellite Derived Emissions and Crop Yield Based Approaches

416   In Section 4.3, it was noted that annual emissions totals calculated using crop yield based approaches (CYBAs) are
417   greater than those calculated using the VIIRS-IM/Him method by a factor of 2-3, depending on species. We believe
418   that this discrepancy relates to the 'burning ratio' (BR) used in CYBA to produce emissions estimates. The burning
419   ratio is the ratio of crop residue burned in the field compared to the total amount of residue produced by harvesting,
420   and is a key parameter in bottom up CYBAs (see Eqn. 1, and Chen *et al.,* 2017; Gao *et al.,* 2002; Huang *et al.,* 2012;
421   Li *et al.,* 2016). Streets *et al.* (2003) used a uniform BR of 17 % derived from 1970's data, however more recent
422   studies often make use of regionally varying fractions. We identified three sources of regionally varying burning ratios
423   that are widely used in the CYBA literature:

424	i)	Wang and Zhang (2008), divided all provinces in China into six zones according to their geographical
425		distribution. A questionnaire-based survey conducted amongst farmers within these regions was used to
426		elucidate the level of burning activity, and using the responses it was determined that burning ratios for
427		the different categories ranged from 11% to 33%. Outputs were applied and referenced in a series of fire
428		emission studies (He *et al.,* 2011, Qin and Xie 2011, Zhang *et al.,* 2016).
429	ii)	Gao *et al.* (2002) derived a set of province-dependent burning ratios adopted from a large-scale
430		investigation of crop residue use across different Chinese provinces. These ratios have been used and
431		referenced in Huang *et al.* (2012), Yan *et al.* (2006), Zhang *et al.* (2008), and are shown in Fig. 10.
432	iii)	A derived value based on farmers' income levels, based on the fact that Cao *et al.,* (2006) found a positive
433		linear correlation between the income of farmers and burning ratio (r = 0.81). This relationship has been
434		applied within several fire emission studies (Sun *et al.,* 2016, Zhao *et al.,* 2015) and will be examined in
435		Section 5.4.

436 Using crop yield information and the DMB data derived from the VIIRS-IM/Him processing performed herein, it is

437 straight forward to reverse the CYBA methodology to calculate the burning ratio for each crop type. This procedure

438 can help confirm whether the outputs derived herein are comparable with those of the existing literature, as well as

439 enabling the advantages offered by the remote sensing time series to be fully exploited. The burning ratios (B_{ij}) for

440 each province *i* and crop type *j* are calculated from:

441 $$B_{ij} = \frac{DMB_{ij}}{P_{ij}R_iC} \tag{10}$$

442 Where DMB_{ij} is the estimated VIIRS DMB (g/m^2) for province *j* and crop *i*; P_{ij} is the yield of crop *i* for province *j* (kg);

443 R_i is the dry matter production-to-residue ratio for crop *i* (unitless) and *C* is crop combustion completeness (proportion,

444 0-1). The province level crop yield P_{ij} is derived from annually published statistical reports, and are presented in Table

445 S1. R_i and *C* are from Huang et al., (2012); and are presented in Table S2.

446 The crop and province dependent burning ratios calculated from the VIIRS-IM/Him data are shown in Fig. 10,

447 alongside the burning ratios from Gao *et al.* (2002). Fig. 10 indicates that there is considerable variation in burning

448 ratios between individual provinces, and that VIIRS-IM/Him wheat burning ratios for are clearly much higher than

449 rice/corn burning ratios. When averaged over the entire Eastern China study area, yearly mean burning ratios from

450 our results for wheat are highest (7.8 - 12%), followed by corn (1.7 - 2.3%), then rice (0.9 - 2.0%). Equivalent mean

451 burning ratios calculated using data from Gao *et al.* (2002) are 9.8 %, 5.9 % and 8.5 %, respectively. While VIIRS-

452 IM/Him wheat residue burning ratios are in reasonable agreement with those used in the various CYBA studies, our

453 rice and corn burning ratios are much lower; this appears to explain why total annual emissions from the VIIRS-

454 IM/Him approach are much lower than the total emissions obtained from the CYBA studies.

455 Fig. 10 also indicates that burning ratios are not only influenced by crop type and province, but also vary considerably

456 from year to year. For example, in 2012, satellite derived wheat burning ratios for the important agricultural provinces

457 of Anhui (30%), Shandong (11%), Jiangsu (24%) and Henan (11%) are not dissimilar to corresponding ratios (20%,

458   8%, 10%, 7% respectively) from Gao *et al.,* (2002). However, during 2015, values derived in this study are much

459   lower (Anhui = 6 %; Shandong = 4 %; Jiangsu = 4 %; Henan = 6 %). This interannual variation may be linked with

460   changing local farming activity and prohibition policies (Chen *et al.,* 2017, Li *et al.,* 2016, Yang *et al.,* 2008).

461   We believe that the disagreement between the burning ratios derived here and those used in CYBA derived studies

462   indicate that emissions inventories derived using traditional CYBAs may be overestimating agricultural burning

463   emissions, for two main reasons: (1) there appears to be considerable uncertainty and subjectivity associated with the

464   methods used to estimating burning ratios used in CYBA studies, and (2) many burning ratios used in CYBA studies

465   are taken from relatively old (>5-10 years) sources of data. For example, Street *et al.* (2003) use data from 1970's,

466   while most later researchers use burning ratios from Wang and Zhang (2008) and Gao *et al*. (2002) as listed above in

467   this section.

468   As shown by this analysis, burning ratios appear to be subject to high spatial and interannual variability due to rapidly

469   changing agricultural policies and decision making that influences the fate of crop residues. As such, in order to ensure

470   reliable emissions estimates, we suggest that future agricultural emission studies and inventories that are based upon

471   CYBAs should endeavour to use burning ratios derived from data (1) with high granularity, and (2) that was collected

472   in the corresponding inventory year.

473

474   5.4 Influence of Social Factors on Agricultural Burning

475   As highlighted in Section 5.2, some studies assume a positive relationship between burning ratio and the mean local

476   income of farmers (Cao *et al.,* 2006; Qin and Xie, 2011). The explanation for this is that higher income areas have

477   better access to electricity and other energy sources, and thus have less need to utilise crop residues for heating and

478   cooking – leading to higher ratios of open burning at these locations. However, this is not what we observe in from

479   analyses carried out for this study. In Fig. 11a, minimal correlation was found between GDP and burning ratio, and

480   there is some suggestion of an inverse relationship between these variables ($y=-89x+9542$, $r^2=0.13$). When directly

481   comparing GDP with DMB, as Fig. 12 demonstrates, the provinces with the highest average annual DMB per m^2

482   (Anhui and Henan; 46 and 27 $g.m^{-2}.yr^{-1}$ respectively) have lower GDP values (US\$ 5,580 and 5,335 per capita) than

483   provinces with lower annual DMB densities (e.g. Shandong and Jiangsu, with 15 and 21 $g.m^{-2}.yr^{-1}$ respectively) but

484   high GDP per capita (USD\$ 9,882 and 13,311 respectively). In fact, across the eastern China study area, our annual

485   total DMB metric was found to be somewhat inversely correlated with GDP per capita ($r^2 = 0.33$; Fig. 11b).

486   We theorise that the observed inverse correlation between GDP and DMB results from the fact that alternative residue

487   disposal methods to biomass burning have a relatively high cost, and can only be afforded by wealthier

488   farmers/provinces. For example, the local government of Jiangsu Province (a relatively wealthy province [\$ 13,311

489   per capita] with only moderate DMB [21 $g.m^{-2}.yr^{-1}$]) released a regulation in 2009 stating that by the end of 2012, over

490   35% of crop residues should been incorporated into the soil after mechanised harvesting. The regulation also indicated

491   that the local government should include a budget for improving the efficiency of agricultural machinery and subsidise

492   farmers who follow this regulation. Furthermore, alternative uses for crop residues are often expensive, and are likely

493   only a viable option in relatively wealthy areas. For example, research on residue burning for power generation shows

494   the government needs to pay at least 20% of the total cost of the operation to keep the power plants running, partly

495   because of the high costs associated with residue collection and transportation from the fields (Li and Hu, 2009).

496   In addition to influencing the quantity of material burned and when it is burned, societal factors also appear influence

497   the spatial pattern of burning within provinces, and at more granular levels such as at the 0.1° grid cell level. The work

498   presented in Section 5.1 suggests that the winter burning season (Nov-Dec) is caused by delayed burning of residues

499   left over from the autumn harvest season, because of prohibition policies related to burning being more robustly

500   enforced earlier in the season. Fig. 6 also showed that the spatial distribution of FRE areal density during winter is

501   different from the normal autumn burning season that occurs in Sep-Oct. Generally, the areas of strongest burning are

502   further from the provincial capital cities (marked by the green stars in Fig. 6) during autumn. For example, fires in

503   Anhui Province are mainly distributed in the north during autumn, whilst fire locations change to the south (closer to

504   the capital city of Hefei) during the delayed winter burns. A similar example can also be seen in Hubei Province,

505   where fires shift from west to east from the autumn to winter burning seasons.

506   To examine this in a more quantitative manner, we calculated the distance from each grid cell shown in Fig. 6 to their

507   provincial capitals. Fig. 13 shows the normalised frequency distribution of the distance from the capital to the top 10%

508   of FRE releasing grid cells in each province, using data from the four burning seasons during the 2012-2015 period.

509   The first and third distance quartiles during the autumn season are 109 km and 214 km respectively, but for the 'lagged'

510   winter burning season, the distribution shifts to far shorter distances (first and third quartiles of 70 km and 153 km

511   respectively). Similarly, the mean distance from provincial capitals also decreased from 165 km in autumn to 124 km

512   in winter. A Kolmogorov–Smirnov (K-S) test was performed to evaluate the difference between the distributions of

513   distance data for the autumn and winter burning seasons, and the resulting high K-S statistic ($0.30, p < 0.001$) indicates

514   that the distribution of distances during the winter months is substantially different to the autumn distance distribution.

515   Similar results were found when we applied the K-S test to each calendar year of data separately (not shown). One

516   possible explanation for this observed difference is that the geographical shift might also be linked with the policies

517   aimed at prohibiting burning, since areas close to capital cities are likely to have more resources for enforcing the

518   prohibition compared to areas more distant from the major urban populations.

519

520

6. SUMMARY AND CONCLUSION

522   We have developed a new state-of-the-art agricultural burning emissions inventory ('VIIRS-IM/Him') for eastern

523   China by combining fire radiative power (FRP) observations from the VIIRS and Himawari-8 sensors for the 2012-

524   2015 period. While several other studies have also used satellite EO data to develop such inventories, they have all

525   relied on MODIS fire products for their source observations. Such inventories include the global GFED and GFAS

526   inventories, several Chinese regional studies (e.g. Huang et al., 2012, Liu et al., 2015). MODIS fire products are

527   known to show very high omission rates in environments dominated by small agricultural fires (Randerson et al., 2012;

528   Zhang et al., 2017, 2018), but the 'small fire optimised' VIIRS-IM product of Zhang et al. (2017) used in this study

529   detects far more of the fire activity across eastern China and on average show FRP totals around 4x higher than those

530   of the MODIS AF products. To convert the twice-daily VIIRS-IM FRP product information to daily time-integrated

531   FRE, we have used new diurnal fire cycle data from Himawari-8, a geostationary satellite positioned over east Asia

532   that can best capture the specific diurnal fire variability of the agricultural burning regions.

533   Our final VIIRS/Him agricultural fire emissions inventory reports dry matter burned (DMB) totals around 2-5× higher

534   than is reported by GFAS and GFED 4.1s in eastern China for corresponding time periods. Use of a crop rotation map

535   allowed our VIIRS-IM/Him fire and emissions outputs to be disaggregated by individual crop types, and we found

536   wheat residue burning to be the primary agricultural emission source, accounting for over 50% of the total emissions

537   each year for all investigated smoke constituents (CO_2, CO, $PM_{2.5}$ and black carbon). A strong seasonal variation in

538   fire activity and emissions is seen, with annual peak activity occurring in summer (May-June) as a result of wheat

539   residue burning, and a smaller secondary activity peak occurring in autumn (Sept-Oct) as a result of corn and rice

540   residue burning. Furthermore, we discovered a new winter (Nov-Dec) agricultural residue burning season. As no crop

541   harvesting occurs during winter, we suspect that this fire activity results from farmers burning previously stored

542   residues from the autumn harvest in winter, after autumn residue burning prohibitions have been lifted. This theory is

543   supported by our observation of statistically distinct spatial burning patterns in the autumn and winter seasons; the

544   majority of autumn burning occurs at a greater distance from provincial capitals than the winter burning does. This

545   may reflect stronger enforcement of autumn residue burning prohibition measures in close proximity to major urban

546   population centres than in rural locations. Farmers in areas with stronger prohibition enforcement (typically closer to

547   urban areas) then burn their agricultural residue in winter.

548   Detailed comparison to existing inventories showed that our VIIRS-IM/Him annual emissions totals are 1.2-4.7×

549   greater than those reported by GFAS, and 0.5-1.7x those reported by GFED4.1s, with some inter-species variability

550   due to the use of different emissions factors between the inventories. By contrast, the VIIRS-IM/Him inventory shows

551   emissions totals that are on average lower than those from emission inventories derived using crop yield based

552   approaches (CYBA) by a factor of 2-5x. This discrepancy is believed to be primarily due to many CYBAs using

553   outdated and/or inappropriate burning ratios, that consequently leads to CYBAs overestimating the amount of crop

554   residue DMB annually. Back calculated burning ratios from the VIIRS-IM/Him data suggest that burning ratios for

555   rice and corn are much lower than the CYBA literature suggests (approx. 0.9-2.3 % rather than 11-33 %). We also

556   noted considerable inter-provincial and interannual variation in these back calculated burning ratios, for example,

557   wheat burning ratios significantly decrease over our four-year study period. This strongly suggests that high spatial

558   resolution, up-to-date burning ratios should always be used in CYBA for agricultural burning fire emission estimation.

559   Furthermore, several CYBA approaches (e.g. Sun *et al.,* 2016, Zhao *et al.,* 2015) have derived burning ratios from

560   provincial GDP data, assuming a positive relationship between these variables (Cao *et al.,* 2006). However, we found

561   evidence of an opposite (i.e. negative) relationship between provincial GDP and the amount of DMB in agricultural

562   fires, hypothesised to be due to the higher cost of disposal of crop residues by non-biomass burning methods. This

563   suggests that great care needs to be taken when deriving burning ratios for use in future agricultural emissions

Atmospheric
Chemistry
and Physics
Discussions

564   inventories based upon CYBA methods, and that satellite remote sensing approaches based on EO datasets that
565   adequately detect the presence of agricultural fires are a far better approach to fire emissions estimation in such
566   environments.

567

568

576

577   **REFERENCES**

578 Andela, N., Kaiser, J.W., Van der Werf, G.R. and Wooster, M.J., 2015. New fire diurnal cycle characterizations to improve fire
579   radiative energy assessments made from MODIS observations. Atmospheric Chemistry and Physics, 15(15), pp.8831-8846.
580 Andreae, M. O. & Merlet, P. 2001. Emission of trace gases and aerosols from biomass burning. Global biogeochemical cycles,
581   15(4), pp 955-966.
582 Bond, T. C., Doherty, S. J., Fahey, D., Forster, P., Berntsen, T., DeAngelo, B., Flanner, M., Ghan, S., Kärcher, B. & Koch, D. 2013.
583   Bounding the role of black carbon in the climate system: A scientific assessment. Journal of Geophysical Research:
584   Atmospheres, 118(11), pp 5380-5552.
585 Cao, G., Zhang, X. & Zheng, F. 2006. Inventory of black carbon and organic carbon emissions from China. Atmospheric
586   Environment, 40(34), pp 6516-6527.
587 Chan, C. K. & Yao, X. 2008. Air pollution in mega cities in China. Atmospheric Environment, 42(1), pp 1-42.
588 Cheng, Y., Engling, G., He, K. B., Duan, F. K., Ma, Y. L., Du, Z. Y., Liu, J. M., Zheng, M. & Weber, R. J. 2013. Biomass burning
589   contribution to Beijing aerosol. Atmos. Chem. Phys., 13(15), pp 7765-7781.
590 Chen, J., Chen, J., Liao, A., Cao, X., Chen, L., Chen, X., He, C., Han, G., Peng, S., Lu, M., Zhang, W., Tong, X., Mills, J., 2015.
591   Global land cover mapping at 30m resolution: A POK-based operational approach. ISPRS J. Photogramm. Remote Sens.,
592   Global Land Cover Mapping and Monitoring 103, 7–27. https://doi.org/10.1016/j.isprsjprs.2014.09.002
593 Chen, J., Li, C., Ristovski, Z., Milic, A., Gu, Y., Islam, M.S., Wang, S., Hao, J., Zhang, H., He, C. and Guo, H., 2017. A review of
594   biomass burning: Emissions and impacts on air quality, health and climate in China. Science of the Total Environment.
595 Du, H., Kong, L., Cheng, T., Chen, J., Du, J., Li, L., Xia, X., Leng, C. & Huang, G. 2011. Insights into summertime haze pollution
596   events over Shanghai based on online water-soluble ionic composition of aerosols. Atmospheric Environment, 45(29), pp
597   5131-5137.
598 Ellicott, E., Vermote, E., Giglio, L. and Roberts, G., 2009. Estimating biomass consumed from fire using MODIS FRE. Geophysical
599   Research Letters, 36(13).
600 Freeborn, P. H., Wooster, M. J., Hao, W. M., Ryan, C. A., Nordgren, B. L., Baker, S. P. & Ichoku, C. 2008. Relationships between
601   energy release, fuel mass loss, and trace gas and aerosol emissions during laboratory biomass fires. Journal of Geophysical
602   Research: Atmospheres, 113(D1), pp D01301.
603 Fu, J. Y., Jiang, D., Huang, Y. H., 2014a. 1-km grid population dataset of China, Global Change Research Data
604   Publishing & Repository, DOI:10.3974/geodb.2014.01.06.V1
605 Fu, J. Y., Jiang, D., Huang, Y. H., 2014b. 1-km grid GDP dataset of China, Global Change Research Data Publishing
606   & Repository, DOI:10.3974/geodb.2014.01.07.V1Gao, X., Ma, W., Ma, C., Zhang, F., Wang, Y., 2002. Analysis of the
607   current status of utilization of crop straw in China. Journal of Huazhong Agricultural University 21, 242–247 (in Chinese).
608 Giglio, L., Csiszar, I. & Justice, C. 2006. Global distribution and seasonality of active fires as observed with the Terra and Aqua
609   Moderate Resolution Imaging Spectroradiometer (MODIS) sensors. J. Geophys. Res, 111(G02016.

610   Giglio, L., Randerson, J.T. and Werf, G.R., 2013. Analysis of daily, monthly, and annual burned area using the fourth-generation
611   global fire emissions database (GFED4). Journal of Geophysical Research: Biogeosciences, 118(1), pp.317-328.
612   Goldberg, M.D., Kilcoyne, H., Cikanek, H., Mehta, A., 2013. Joint Polar Satellite System: The United States next generation
613   civilian polar-orbiting environmental satellite system. J. Geophys. Res. Atmospheres 118, 13,463-13,475.
614   https://doi.org/10.1002/2013JD020389
615   He, M., Zheng, J., Yin, S. & Zhang, Y. 2011. Trends, temporal and spatial characteristics, and uncertainties in biomass burning
616   emissions in the Pearl River Delta, China. Atmospheric Environment, 45(24), pp 4051-4059.
617   Huang, X., Li, M., Li, J. & Song, Y. 2012. A high-resolution emission inventory of crop burning in fields in China based on MODIS
618   Thermal Anomalies/Fire products. Atmospheric Environment, 50(0), pp 9-15.
619   Jiang, D., Zhuang, D., Fu, J., Huang, Y. & Wen, K. 2012. Bioenergy potential from crop residues in China: Availability and
620   distribution. Renewable and Sustainable Energy Reviews, 16(3), pp 1377-1382.
621   Kaiser, J. W., Heil, A., Andreae, M. O., Benedetti, A., Chubarova, N., Jones, L., Morcrette, J. J., Razinger, M., Schultz, M. G.,
622   Suttie, M. & van der Werf, G. R. 2012. Biomass burning emissions estimated with a global fire assimilation system based
623   on observed fire radiative power. Biogeosciences, 9(1), pp 527-554.
624   Li, W., Shao, L. & Buseck, P. 2010. Haze types in Beijing and the influence of agricultural biomass burning. Atmospheric
625   Chemistry and Physics, 10(17), pp 8119-8130.
626   Li, J.F. and Hu, Y.S., 2009. Analysis on investment and operation of straw-fired power plants in Jiangsu province. Electric power
627   technologic economics, 5, p.005 (in Chinese).
628   Li, J., Li, Y., Bo, Y. and Xie, S., 2016. High-resolution historical emission inventories of crop residue burning in fields in China
629   for the period 1990–2013. Atmospheric Environment, 138, pp.152-161.
630   Li, M., Q. Zhang, D. Streets, K. B. He, Y. F. Cheng, L. K. Emmons, H. Huo, S. C. Kang, Z. Lu, M. Shao, H. Su, X. Yu, and Y.
631   Zhang (2014), Mapping Asian anthropogenic emissions of non-methane volatile organic compounds to multiple chemical
632   mechanisms, Atmos. Chem. Phys., 14, 5617-5638.
633   Liu, M., Song, Y., Yao, H., Kang, Y., Li, M., Huang, X. and Hu, M., 2015. Estimating emissions from agricultural fires in the
634   North China Plain based on MODIS fire radiative power. Atmospheric environment, 112, pp.326-334.
635   Liu, H., Jiang, G. M., Zhuang, H. Y. & Wang, K. J. 2008. Distribution, utilization structure and potential of biomass resources in
636   rural China: With special references of crop residues. Renewable and Sustainable Energy Reviews, 12(5), pp 1402-1418.
637   NBSC (National Bureau of Statistic of China) China Statistical Yearbook, 480 2003–2015, China Statistics Press, Beijing (2004–
638   2016) (in Chinese).
639   Portmann, F. T., Siebert, S. & Döll, P. 2010. MIRCA2000—Global monthly irrigated and rainfed crop areas around the year 2000:
640   A new high-resolution data set for agricultural and hydrological modeling. Global Biogeochemical Cycles, 24(1).
641   Qin, Y. & Xie, S. D. 2011. Historical estimation of carbonaceous aerosol emissions from biomass open burning in China for the
642   period 1990–2005. Environmental Pollution, 159(12), pp 3316-3323.
643   Randerson, J., Chen, Y., Werf, G., Rogers, B. & Morton, D. 2012. Global burned area and biomass burning emissions from small
644   fires. Journal of Geophysical Research: Biogeosciences (2005–2012), 117(G4), pp.
645   Roberts, G., Wooster, M.J. and Lagoudakis, E., 2009. Annual and diurnal african biomass burning temporal dynamics.
646   Biogeosciences, 6(5), pp.849-866.
647   Roberts, G., Wooster, M.J., Xu, W., Freeborn, P.H., Morcrette, J.J., Jones, L., Benedetti, A. and Kaiser, J., 2015. LSA SAF Meteosat
648   FRP Products: Part 2--Evaluation and demonstration of use in the Copernicus Atmosphere Monitoring Service (CAMS).
649   Atmospheric Chemistry & Physics Discussions, 15(12).
650   Schroeder, W., Oliva, P., Giglio, L. and Csiszar, I.A., 2014. The New VIIRS 375 m active fire detection data product: Algorithm
651   description and initial assessment. Remote Sensing of Environment, 143, pp.85-96.
652   Streets, D.G., Yarber, K.F., Woo, J.H. and Carmichael, G.R., 2003. Biomass burning in Asia: Annual and seasonal estimates and
653   atmospheric emissions. Global Biogeochemical Cycles, 17(4).
654   Sun, J., Peng, H., Chen, J., Wang, X., Wei, M., Li, W., Yang, L., Zhang, Q., Wang, W. & Mellouki, A. 2016. An estimation of
655   CO2 emission via agricultural crop residue open field burning in China from 1996 to 2013. Journal of Cleaner Production,
656   112, Part 4(2625-2631.
657   van der Werf, G. R., Randerson, J. T., Giglio, L., Collatz, G. J., Mu, M., Kasibhatla, P. S., Morton, D. C., DeFries, R. S., Jin, Y. &
658   van Leeuwen, T. T. 2010. Global fire emissions and the contribution of deforestation, savanna, forest, agricultural, and peat
659   fires (1997–2009). Atmos. Chem. Phys., 10(23), pp 11707-11735.
660   van der Werf, G. R., Randerson, J. T., Giglio, L., van Leeuwen, T. T., Chen, Y., Rogers, B. M., Mu, M., van Marle, M. J. E.,
661   Morton, D. C., Collatz, G. J., Yokelson, R. J., and Kasibhatla, P. S.: Global fire emissions estimates during 1997–2016,
662   Earth Syst. Sci. Data, 9, 697-720, https://doi.org/10.5194/essd-9-697-2017, 2017.
663   Wang & Zhang, 2016, http://news.chengdu.cn/2016/1106/1829718.shtml,Chengdu Business Daily
664   Wang, S. & Zhang, C. 2008. Spatial and temporal distribution of air pollutant emissions from open burning of crop residues in
665   China. Sciencepaper online, 3(5), pp 329-333.
666   Wolfe, R.E., Lin, G., Nishihama, M., Tewari, K.P., Tilton, J.C. and Isaacman, A.R., 2013. Suomi NPP VIIRS prelaunch and on-
667   orbit geometric calibration and characterization. Journal of Geophysical Research: Atmospheres, 118(20), pp.11-508.
668   Wooster, M. J., Roberts, G., Perry, G. L. W. & Kaufman, Y. J. 2005. Retrieval of biomass combustion rates and totals from fire
669   radiative power observations: FRP derivation and calibration relationships between biomass consumption and fire radiative
670   energy release. Journal of Geophysical Research: Atmospheres, 110(D24), pp D24311.

671 Xu, W., Wooster, M.J., Kaneko, T., He, J., Zhang, T. and Fisher, D., 2017. Major advances in geostationary fire radiative power
672   (FRP) retrieval over Asia and Australia stemming from use of Himarawi-8 AHI. Remote Sensing of Environment, 193,
673   pp.138-149.
674 Yamaji, K., Li, J., Uno, I., Kanaya, Y., Irie, H., Takigawa, M., Komazaki, Y., Pochanart, P., Liu, Y., Tanimoto, H., Ohara, T., Yan,
675   X., Wang, Z. & Akimoto, H. 2010. Impact of open crop residual burning on air quality over Central Eastern China during
676   the Mount Tai Experiment 2006 (MTX2006). Atmos. Chem. Phys., 10(15), pp 7353-7368.
677 Yan, X., Ohara, T. & Akimoto, H. 2006. Bottom-up estimate of biomass burning in mainland China. Atmospheric Environment,
678   40(27), pp 5262-5273.
679 Yang, S., He, H., Lu, S., Chen, D. & Zhu, J. 2008. Quantification of crop residue burning in the field and its influence on ambient
680   air quality in Suqian, China. Atmospheric Environment, 42(9), pp 1961-1969.
681 Za, 2015, http://www.chinanews.com/sh/2015/11-04/7606112.shtml, Legislative Evening Newspaper
682 Zhang, H., Ye, X., Cheng, T., Chen, J., Yang, X., Wang, L. & Zhang, R. 2008. A laboratory study of agricultural crop residue
683   combustion in China: Emission factors and emission inventory. Atmospheric Environment, 42(36), pp 8432-8441.
684 Zhang, L., Liu, Y. and Hao, L., 2016. Contributions of open crop straw burning emissions to PM2. 5 concentrations in China.
685   Environmental Research Letters, 11(1), p.014014.
686 Zhang, T., Wooster, M.J., Green, D.C. and Main, B., 2015. New field-based agricultural biomass burning trace gas, PM2. 5, and
687   black carbon emission ratios and factors measured in situ at crop residue fires in Eastern China. Atmospheric
688   Environment, 121, pp.22-34.
689 Zhang, T., Wooster, M.J. and Xu, W., 2017. Approaches for synergistically exploiting VIIRS I-and M-Band data in regional active
690   fire detection and FRP assessment: A demonstration with respect to agricultural residue burning in Eastern China. Remote
691   sensing of environment, 198, pp.407-424.
692 Zhang, T., Wooster, M., de Jong, M. and Xu, W., 2018. How Well Does the 'Small Fire Boost'Methodology Used within the
693   GFED4. 1s Fire Emissions Database Represent the Timing, Location and Magnitude of Agricultural Burning?. Remote
694   Sensing, 10(6), p.823.
695 Zhao, H., Tong, D. Q., Gao, C. & Wang, G. 2015. Effect of dramatic land use change on gaseous pollutant emissions from biomass
696   burning in North Eastern China. Atmospheric Research, 153(429-436).
697 Zhou, L., Divakarla, M., Liu, X., Layns, A., Goldberg, M., 2019. An Overview of the Science Performances and
698   Calibration/Validation of Joint Polar Satellite System Operational Products. Remote Sens. 11, 698.
699   https://doi.org/10.3390/rs11060698
700 Zuo 2015, http://www.chinanews.com/gn/2015/12-11/7666514.shtml, Anhui News
701

702 **Table 1:** Emission Factors for agricultural residue burning used in this study. Wheat and rice emission factors were
703 derived from field measurements conducted in eastern China and reported by Zhang et al. (2015), while the corn
704 emission factors are from Andreae and Merlet (2001), the same as those used in GFAS (Kaiser *et al.,* 2012). *$PM_{2.5}$
705 = particulate matter with diameter < 2.5μm
706

	Emissions Factor (g.kg^{-1})		
	Wheat	Corn	Rice
CO_2	1739±19	1308±14	1761±30
CO	60±12	92±18	47±19
$PM_{2.5}$*	6.1±1.3	8.3±1.8	9.6±4.3
Black Carbon	0.70±0.09	0.42±0.05	0.56±0.04

707
708 **Table 2:** Total species-specific fire emissions calculated in this study for agricultural burning in eastern China, and
709 comparison to those contained within other fire emissions inventories and calculated in previous studies.
710

Reference	Region	Year	Method	Emissions (Gg.yr^{-1})			
				CO_2	CO	$PM_{2.5}$	BC
This study	Eastern China	2012	Satellite	31066 ± 1960	1035±327	124±43	11±1.8
		2013		31107 ± 1748	1025±320	130±44	11±1.7
		2014		27069 ± 1421	904±279	107±36	10±1.5
		2015		16932 ± 1044	562±177	70±24	6±0.95
GFAS	Eastern China	2012	Satellite	9219	649	58	3.0
Kaiser *et al.,* 2012		2013		8173	576	52	2.6
		2014		8760	617	55	2.8
		2015		6818	480	43	2.2
GFED4.1s	Eastern China	2012	Satellite	18629	1199	74	8.8
Van der Werf *et al.*, 2017		2013		24034	1547	95	11
		2014		18241	1173	72	8.6

		2015		15892	1023	63	7.5
Liu *et al.,* 2015	NCP[1]	2012	Satellite	26000	1700	102	13
		2013		9800	630	39	5
		2014		13000	820	50	6
Zhang et al., 2008	Eastern China[3]	2004	CYBA[2]	67703	5624	-	-
Huang et al., 2012	Eastern China[3]	2006	CYBA	41374	2668	164	20
Qiu et al., 2016	Eastern China	2013	CYBA	72071	2549	445	42
Li et al., 2016	NCP	2012	CYBA	68675	5983	452	23
Sun et al., 2016	China	2013	CYBA	192540	-	-	-
Street *et al.,* 2003	China	2000	CYBA	160000	10000	-	70
Yan *et al.,* 2006	China	2000	CYBA	184000	11000	470	80

[1] NCP refers to the North China Plain, which has a geographic extent similar to that of this study (32-41ºN, 113-121ºE).
[2] CYBA refers to Crop Yield Based Approaches, see Section 2.6.1
[3] Sum of provinces/cities shown in Fig.1 of this study.
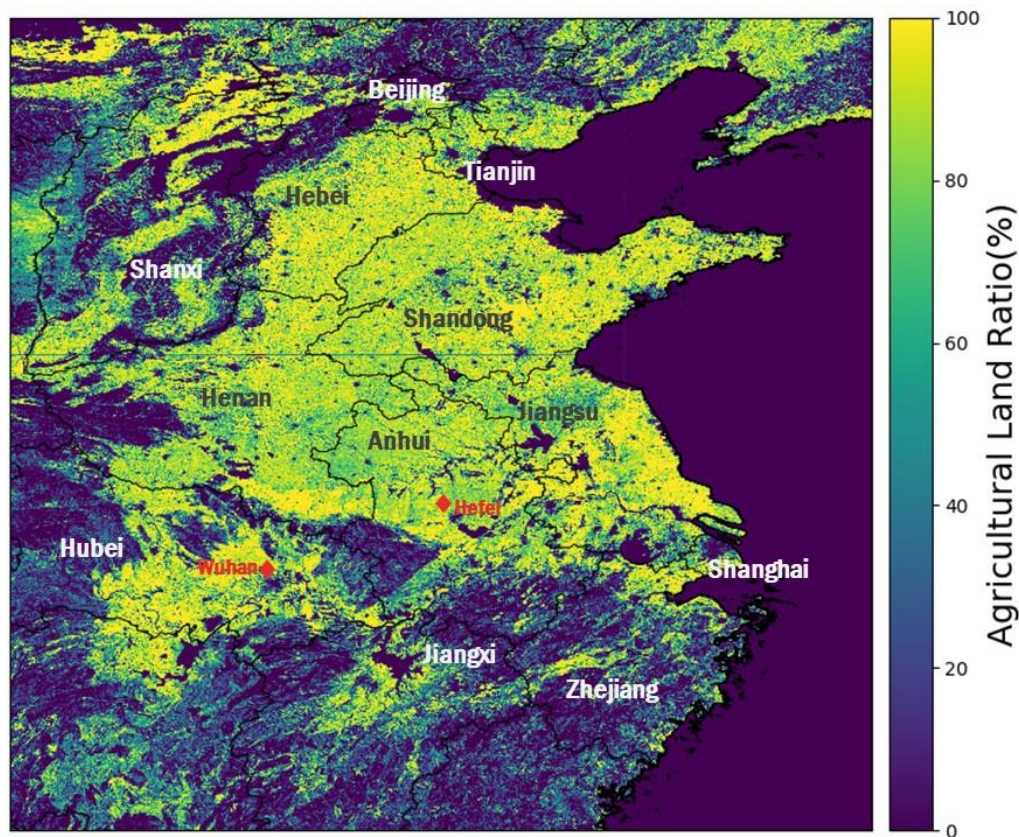
Figure 1: The spatial extent of the study area (111-123° E, 27-40° N). The agricultural land ratio taken from the GlobeLand30 land cover product (Chen et al, 2015) was re-gridded to 0.01 degree spatial resolution, and is overlain with the main provinces, mega-cities and some important provincial capital cities in eastern China. The basic layer of country/province borders within this map was created using Python Basemap librabry.
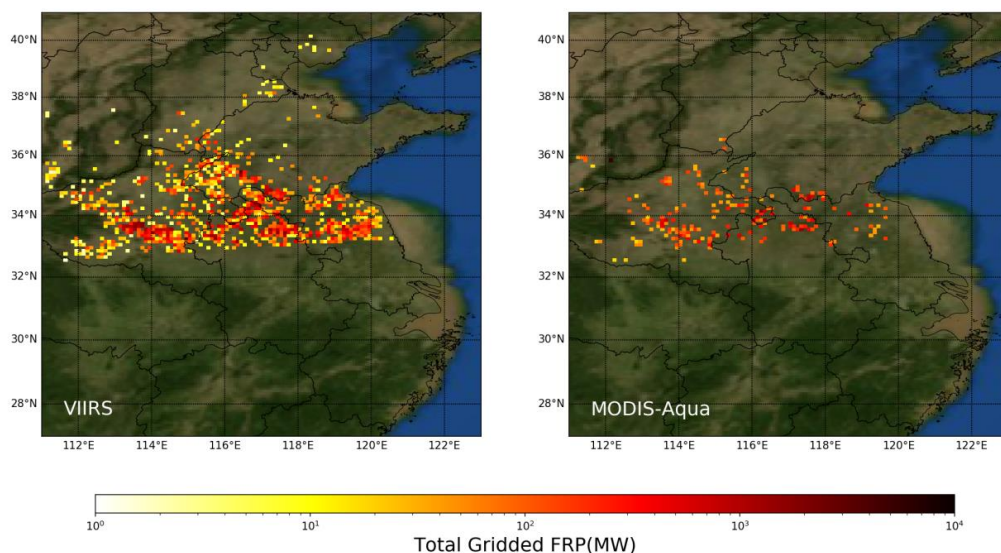
720
**Figure 2:** Example of the spatial distribution of total gridded FRP (MW; calculated per 0.1° grid cell) calculated from
near simultaneous VIIRS-IM and MODIS Aqua data collected over the eastern China study area of Fig. 1 on June
12th, 2012. The VIIRS-IM data product clearly quantifies a higher proportion of the FRP from fires burning in the
region at the time of the satellite overpass than MODIS Aqua does. The basic layer of country/province borders within
this map was created using Python Basemap librabry.
726
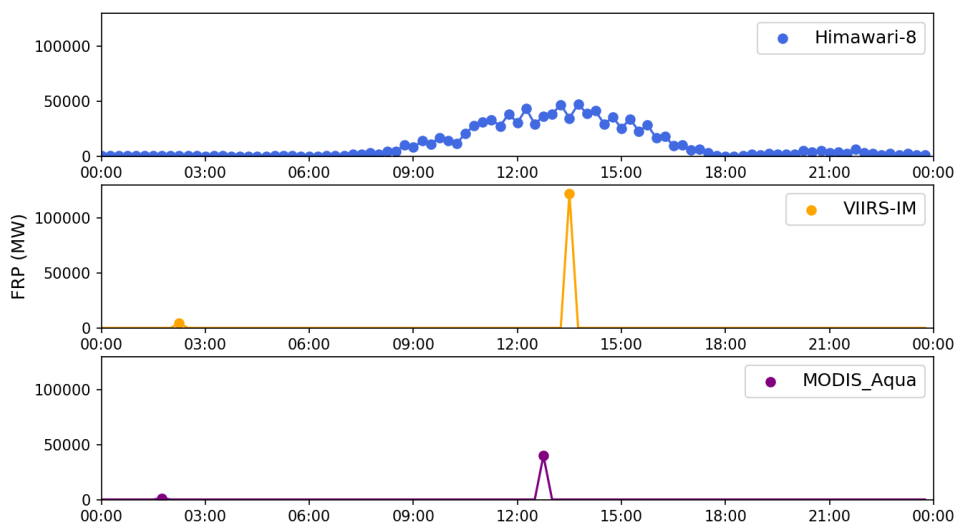
727
728
Figure 3: Time series of spatially summed FRP for eastern China, as retrieved from geostationary Himawari, and
729
polar-orbiting VIIRS-IM and MODIS observations made on June 11th, 2015. VIIRS and MODIS Aqua provide

730   typically two observations per day, and sometimes three when the swath overlaps from different orbits occur.
731   Himawari provides 144 observations per day.
732
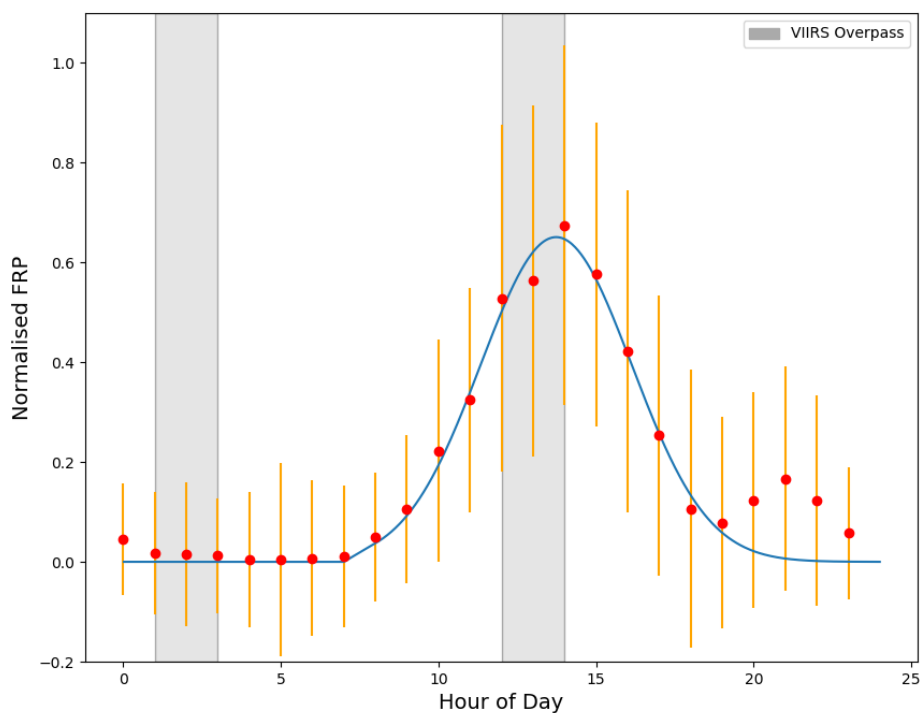
733
734   **Figure 4:** Time series of hourly normalised fire radiative power derived from Himawari-8 FRP data generated using
735   the algorithm of Xu et al. (2017) over eastern China at 0.1 degree for June 2015 (the 'Summer' diurnal fire cycle).
736   The blue curve shows the best fit of the Gaussian distribution, with orange error bar show standard deviation. Grey
737   shading shows the two daily VIIRS overpass periods.
738
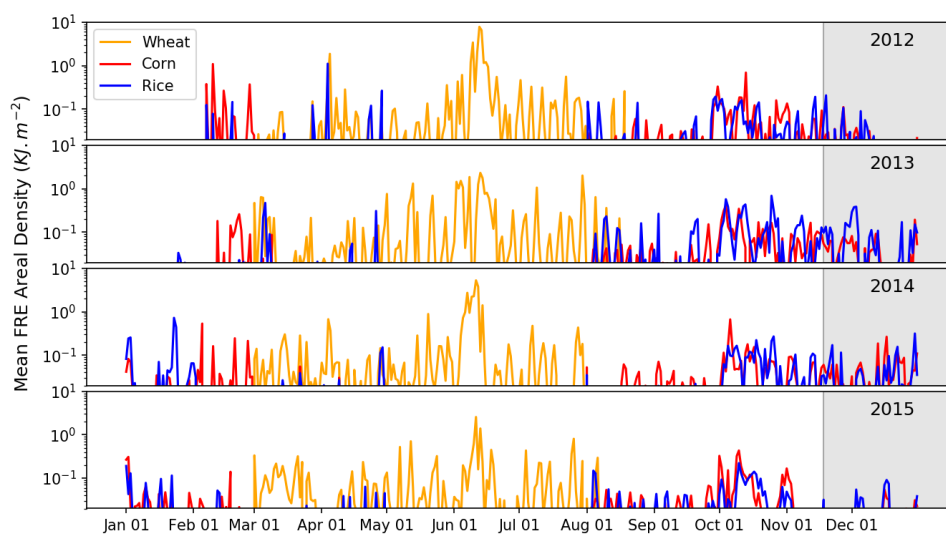
739
Figure 5: Time-series of mean daily FRE areal density (kJ m^{-2}, calculated per 0.1º grid cell) from 2012-2015 for the entire study area disaggregated by crop residue type (wheat, corn and rice) according to the method described in Section 2.4. Grey shaded areas highlighted the usual newly discovered winter burning season from mid-November to December when no crop harvesting occurs but where fires are clearly occurring. This period of agricultural burning is discussed further in Section 5.1
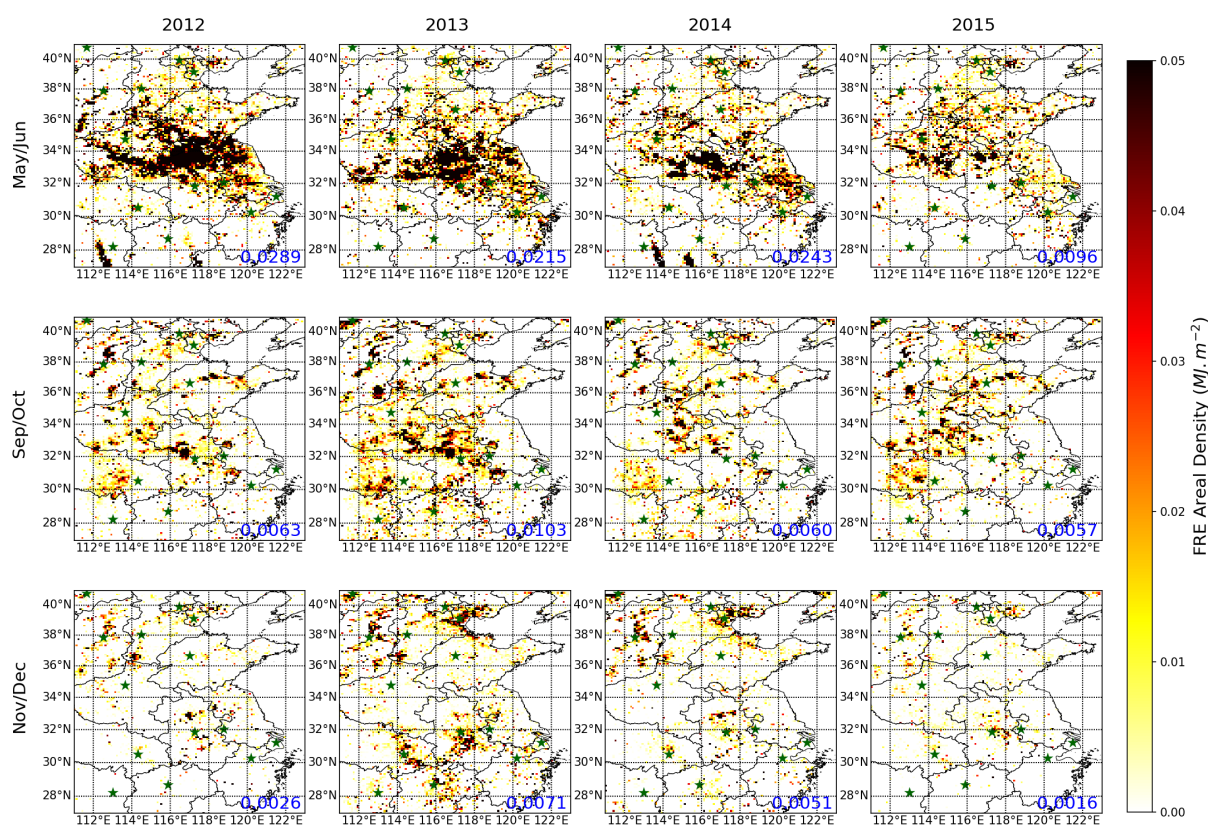
Figure 6: Spatial distribution of FRE areal density (MJ.m^{-2}, 0.1 deg grid cells) for agricultural fires in eastern China from 2012 to 2015 (top to bottom rows) split by fire season: summer (May-June, top row), autumn (Sep-Oct, middle row) and winter (Nov-Dec, bottom row). Mean regional FRE for each season is indicated in blue text, and the capital city location of each province is shown as a green star on each map. The basic layer of country/province borders within this map was created using Python Basemap librabry.
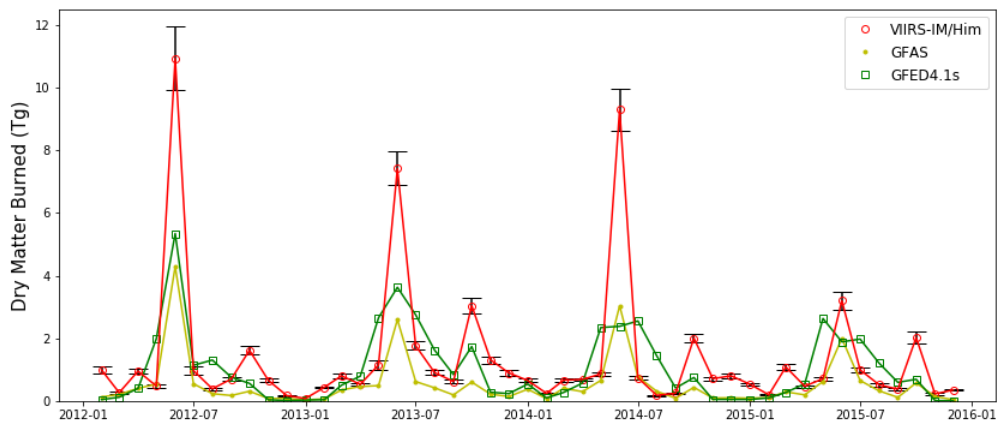
Figure 7: Monthly (2012-2015) time-series of total dry matter burned (DMB) retrieved using the VIIRS-IM/Him FRP product developed in this study (with standard deviation shown as black error bars), along with comparable GFAS and GFED4.1s DMB totals.
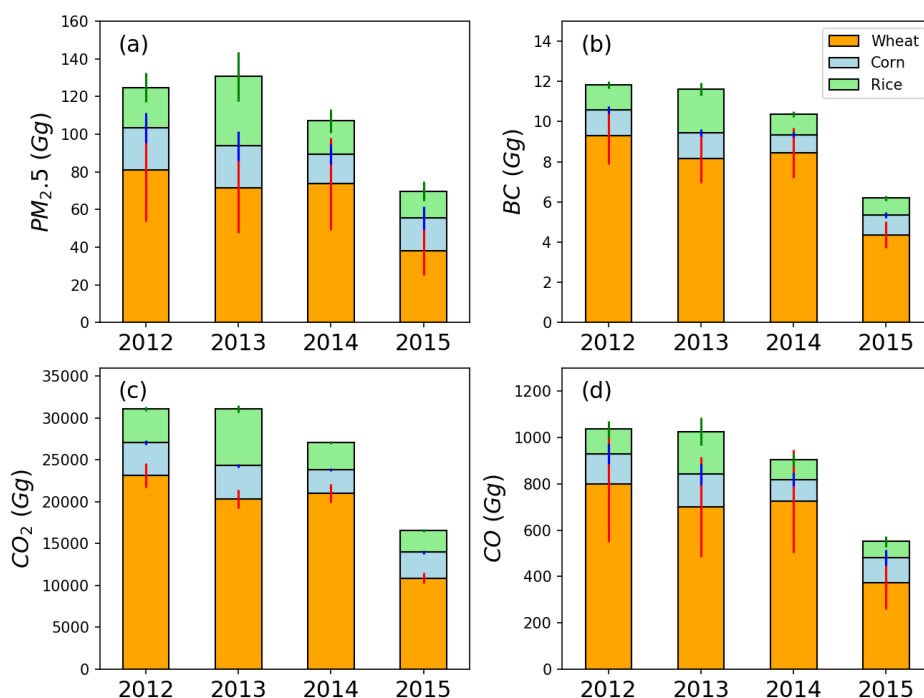
Figure 8: Annual total $PM_{2.5}$, BC, CO_2, and CO emissions for eastern China for the three main crop residues burning types (wheat, corn, rice) calculated for 2012-2015 using the VIIRS-IM/Him based emissions inventory developed herein. Coloured error bars indicate 1 standard deviation.

Atmospheric
Chemistry
and Physics
Discussions
Open Access
EGU
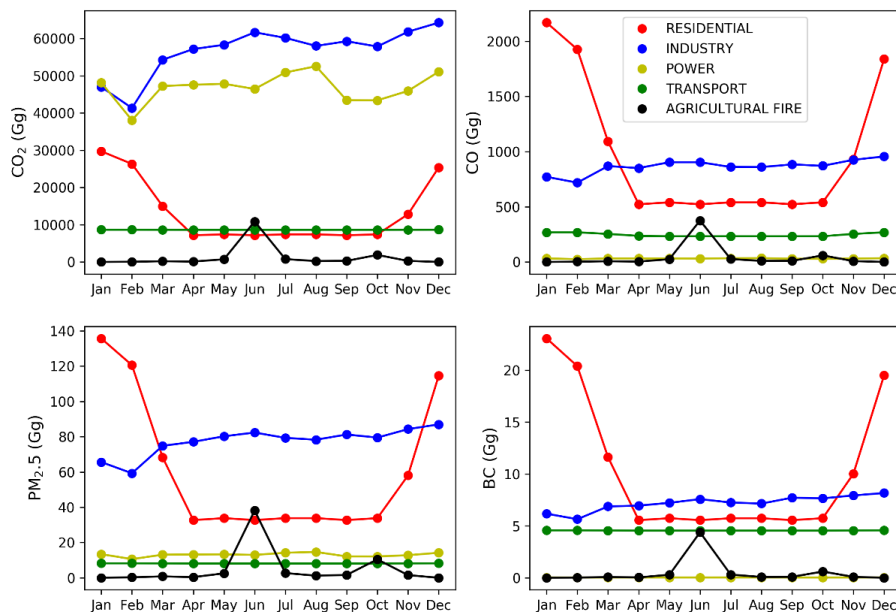
Figure 9: Comparison of monthly CO_2, CO, $PM_{2.5}$ and BC emissions from agricultural fires with those from other emission sources (residential, industry, power, transport, data source: Li et al., 2015) in the intensive burning area (32-36º N, 112-122º E) of eastern China in the year 2013.
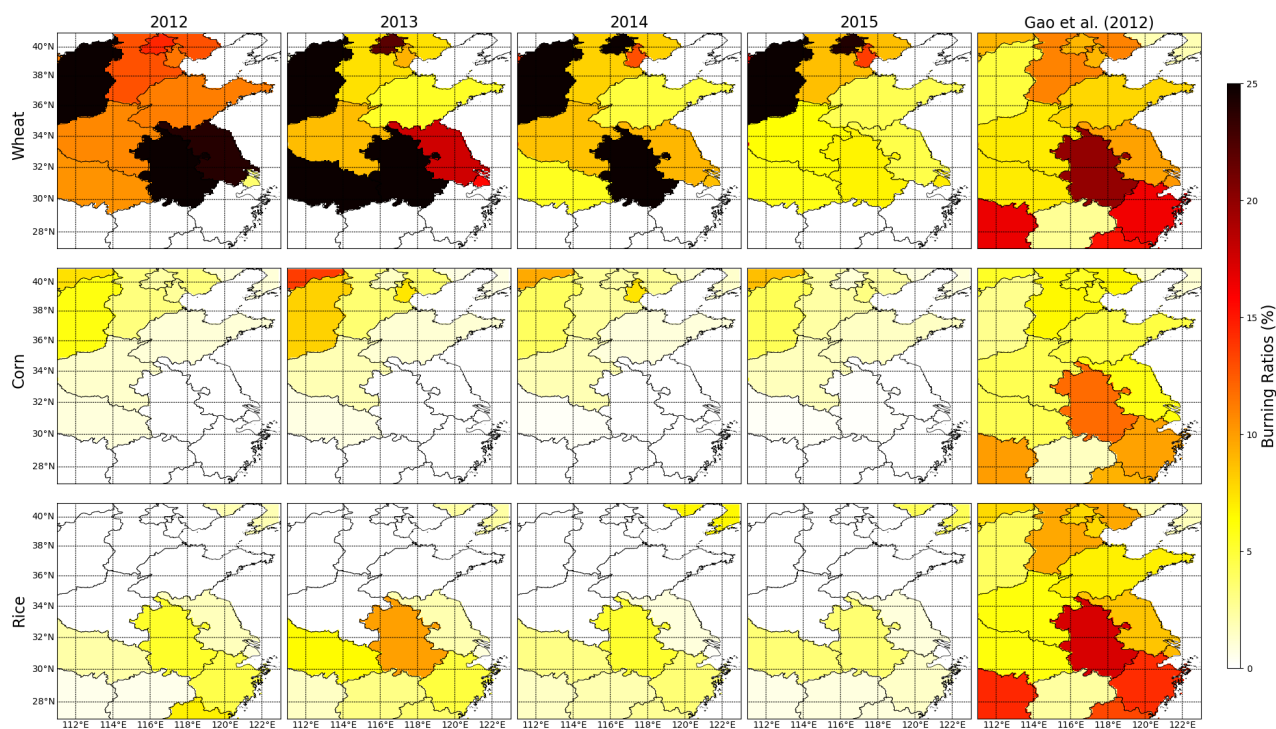
Figure 10: Temporal and spatial variability of province-specific percentages of crop residues burned in the fields (burning ratio metrics) of eastern China. Data are calculated using crop yield estimates from National Bureau of Statistics of China and the dry matter burned totals derived herein using our VIIRS-IM/Him DMB datasets from 2012-2015, and compared to the temporally invariant estimates provided by Gao et al., (2002, final column). The basic layer of country/province borders within this map was created using Python Basemap librabry.
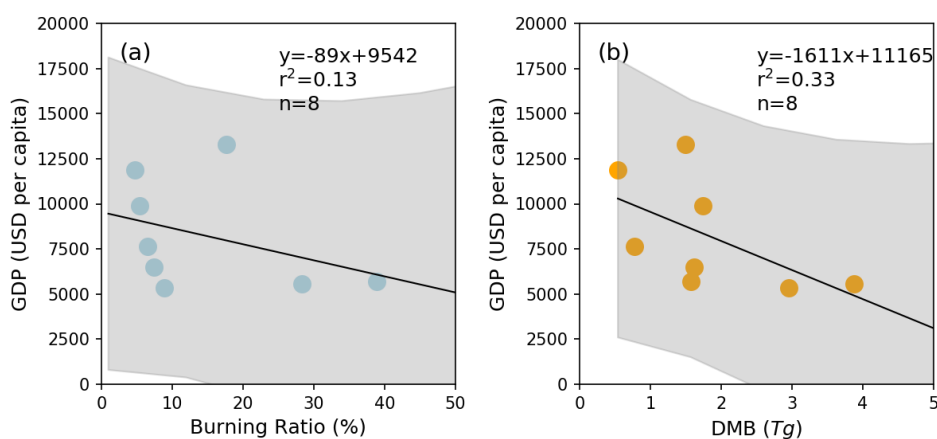
Atmospheric
Chemistry
and Physics
Discussions

Open Access

EGU

Figure 11: Direct comparisons of mean GDP per capita with (a) burning ratio for wheat from 2012, (b) province-specific yearly dry matter burned (DMB). The best fit linear relationships are shown, along with its equation, and the grey shaded area represents the 95% confidence limit on the relationship.
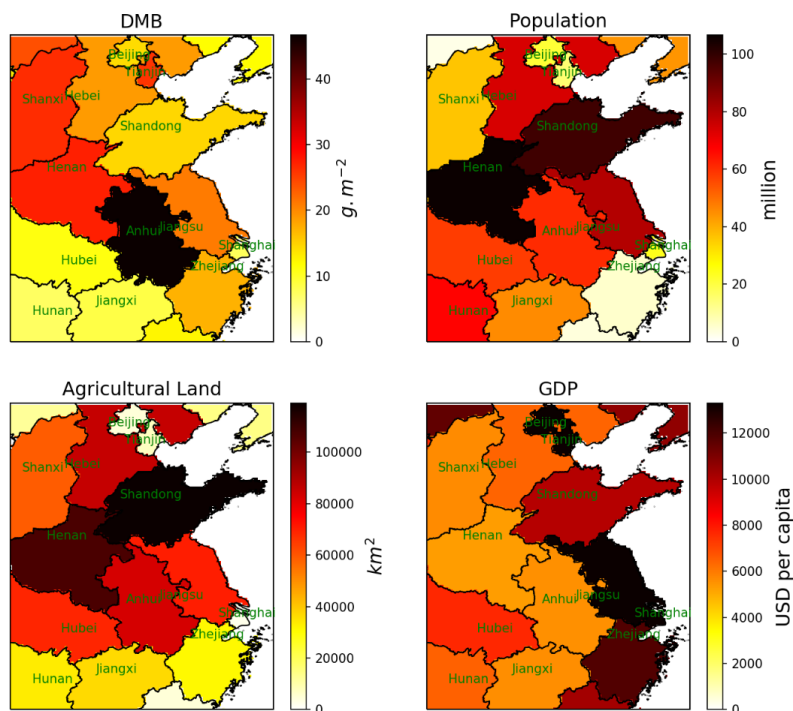

Figure 12: Spatial distribution of province-specific: (a) mean annual dry matter burned as calculated using the VIIRS-IM/Him approach developed herein, (b) population (Data source: Fu *et al.,* 2014a), (c) agricultural land area (Data source: GlobeLand30, http://www.globallandcover.com/) and (d) mean GDP per capita (Data source: Fu *et al.,* 2014b). The basic layer of country/province borders within this map was created using Python Basemap librabry.
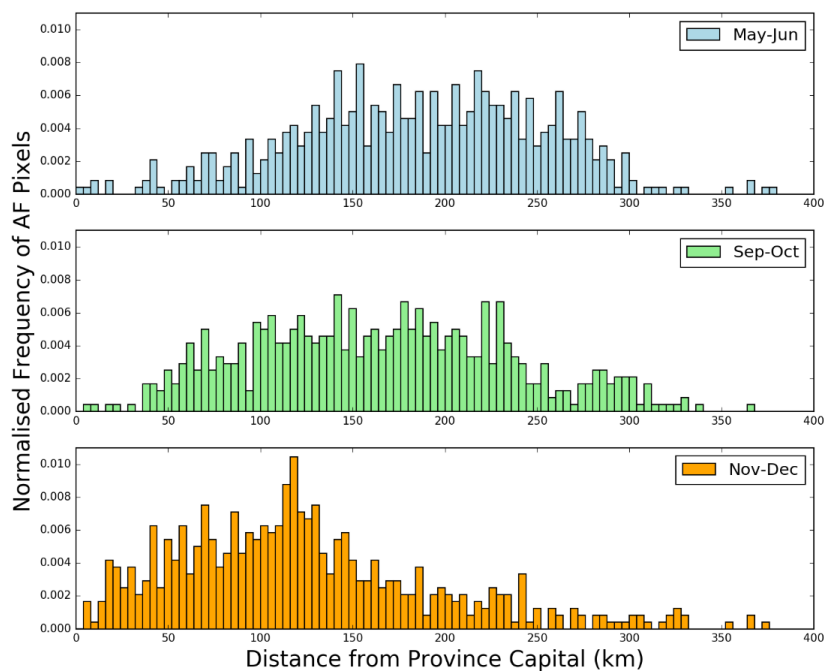
Figure 13: Normalised frequency distribution of distance from province capital of the top 10% of high FRE VIIRS-IM/Him product 0.1 degree grid cells during the three burning seasons: Summer - May to June (top, blue), Autumn – September to October (middle, green), and Winter - November to December (bottom, orange). A clear shift towards the origin can be observed in the Nov-Dec period compared with Sep-Oct.